Inorganic Chemistry
Cite This: Inorg. Chem. 2019, 58, 320−326
Article
pubs.acs.org/IC

High-Temperature Ferrimagnetic Half Metallicity with Wide Spin-up Energy Gap in $NaCu_3Fe_2Os_2O_{12}$

Xiao Wang,[†,‡] Min Liu,[†] Xudong Shen,[†,‡] Zhehong Liu,[†,‡] Zhiwei Hu,[∥] Kai Chen,[⊥] Philippe Ohresser,[⊥] Lucie Nataf,[⊥] François Baudelet,[⊥] Hong-Ji Lin,[#] Chien-Te Chen,[#] Yun-Liang Soo,[#] Yi-feng Yang,*[,†,‡] Changqing Jin,[†,‡] and Youwen Long*[,†,‡,§]

[†]Beijing National Laboratory for Condensed Matter Physics, Institute of Physics, Chinese Academy of Sciences, Beijing 100190, China
[‡]School of Physical Sciences, University of Chinese Academy of Sciences, Beijing 100049, China
[§]Songshan Lake Materials Laboratory, Dongguan, Guangdong 523808, China
[∥]Max Planck Institute for Chemical Physics of Solids, Dresden 01187, Germany
[⊥]Synchrotron SOLEIL, L'Orme des Merisiers, Saint-Aubin, BP 48, 91192 Gif-sur-Yvette, Cedex, France
[#]National Synchrotron Radiation Research Center, Hsinchu 30076, Taiwan, ROC

ABSTRACT: A new oxide $NaCu_3Fe_2Os_2O_{12}$ is synthesized using high pressure and temperature conditions. The Rietveld structural analysis shows that the compound possesses both A- and B-site ordered quadruple perovskite structure in $Pn\bar{3}$ symmetry. The valence states of transition metals are confirmed to be $Cu^{2+}/Fe^{3+}/Os^{5.5+}$. The three transition metals all take part in magnetic interactions and generate strong $Cu^{2+}(\uparrow)Fe^{3+}(\uparrow)Os^{5.5+}(\downarrow)$ ferrimagnetic superexchange interactions with a high Curie temperature about 380 K. Electrical transport measurements suggest its half-metallic properties. The first-principles theoretical calculations demonstrate that the compound has a spin-down conducting band and a spin-up insulating band with a wide energy gap.

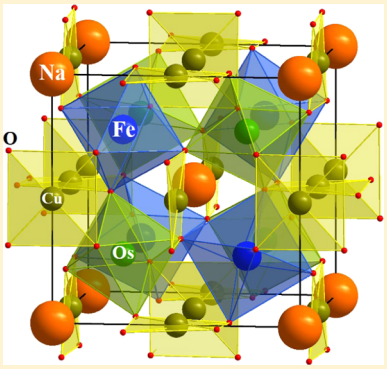

1. INTRODUCTION

Ferromagnetic (FM) or ferrimagnetic (FiM) half metals are a class of very interesting spintronic materials due to their peculiar electronic structure, where only one spin direction is conducting, whereas the other is semiconducting or insulating. As a consequence, the charge carriers near the Fermi level are theoretically 100% spin polarized, giving rise to lots of intriguing magneto-optical and spin-electronic properties.[1−4] In practical applications of half metals, highly spin-polarized conductivity usually occurs at temperatures considerably less than the Curie temperature T_C. Meanwhile, a wider half-metallic energy gap is also desirable to effectively suppress the carriers' spin-flip transition caused by thermal excitation and thereby maintain their half-metallic properties in the working temperature window. It is therefore a pressing requirement in pursuit of magnetic half metals with the T_C being above room temperature and the energy gap being wide enough (e.g., >1.0 eV). In 1983, de Groot et al. reported the first half metal.[5] Since then, a wide variety of half-metallic magnets with different crystal structures were proposed in both experiment and theory.[6−14] However, it is still a big challenge to search for high-performance half metals with potential application near room temperature.

ABO_3 perovskite (Figure 1a) is one of the most widely studied half metals on account of the variable structural derivations and flexible A−B charge combinations. For example, the A-site doped manganese perovskite $La_{0.7}Sr_{0.3}MnO_3$ shows promising half-metallic behavior with Curie temperature as high as 350 K.[15−17] In a perovskite structure, when hybridized 3d−4d or 3d−5d transition metals are introduced into the B sites to form an $A_2BB'O_6$-type ordered double perovskite in a rocksalt-type manner (Figure 1b), a higher magnetic ordering temperature is possibly obtained. Sr_2FeMoO_6 provides a typical example, in which a higher FiM T_C of about 420 K is achieved, and the half-metallic behavior is further revealed by electrical transport measurements and first-principles calculations.[6,18,19] This pioneering work has already stimulated many other studies on B-site ordered perovskite half metals with a higher T_C.[20−24] However, the half-metallic gaps found in these compounds are usually less than 1.0 eV.

As is well known, in ABO_3 or $A_2BB'O_6$ perovskite, the A site often accommodates nonmagnetic alkali, alkali earth, and rare earth ions. Since the ordered B-site substitution of magnetic

Received: August 26, 2018
Published: December 11, 2018

DOI: 10.1021/acs.inorgchem.8b02404
Inorg. Chem. 2019, 58, 320−326

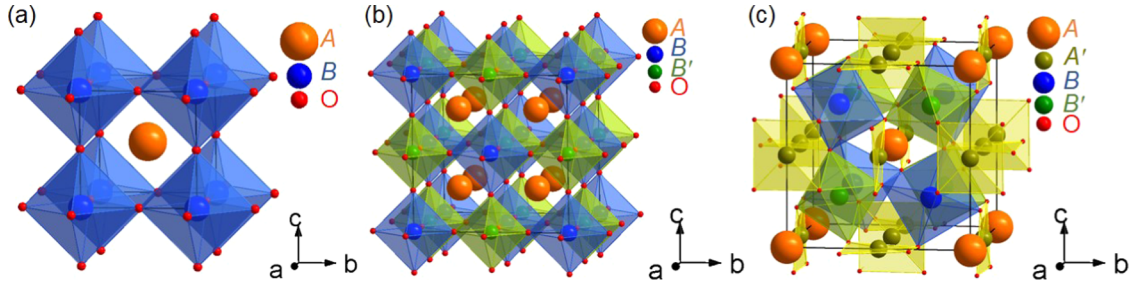

Figure 1. Schematic crystal structures for (a) ABO_3 perovskite, (b) B-site rocksalt-type ordered double perovskite $A_2BB'O_6$, and (c) both A- and B-site ordered quadruple perovskite $AA'_3B_2B'_2O_{12}$.

ions can significantly increase the spin ordering temperature, is it possible to further enhance the T_C by orderly substituting the initially nonmagnetic A-site cation using a magnetic transition metal ion? The quadruple perovskite $AA'_3B_2B'_2O_{12}$ with the orderly distributed A- and B-site provides a unique opportunity for this study. This kind of multiply ordered perovskite crystallizes to the $Pn\bar{3}$ space group (Figure 1c), with cation positions at 2a (0.25, 0.25, 0.25) for the A-site, 6d (0.25, 0.75, 0.75) for the A′-site, 4b (0, 0, 0) for the B-site, and 4c (0.5, 0.5, 0.5) for the B′-site. Since transition metals are present in three different sites (A′, B, and B′) in $AA'_3B_2B'_2O_{12}$, besides the conventional interactions between the B-site, new magnetic and electrical interactions such as A′−A′ and A′−B/B′ can occur, too. The cooperating results of these strong interactions possibly increase the T_C further. As shown in Figure 1c, the crystal structure of $AA'_3B_2B'_2O_{12}$ is composed of $A'O_4$ square planes and $B/B'O_6$ octahedra. Since the $A'O_4$ units are isolated from each other, the corner-sharing $B/B'O_6$ octahedra will dominate the electrical transport properties. Consequently, the magnetism and electrical transport properties of $AA'_3B_2B'_2O_{12}$ can be well tuned by appropriate combinations of transition metals at A′-, B-, and B′-sites, opening up a new avenue to design novel half-metallic magnets with enhanced T_C and considerable half-metallic gap.

Although many ABO_3 and $A_2BB'O_6$ perovskites have already been reported,[25−33] only a few of $AA'_3B_2B'_2O_{12}$ quadruple perovskites with three ordered magnetic ions are discovered,[34−40] because high pressure is often necessary to synthesize these $AA'_3B_2B'_2O_{12}$-type perovskites. Interestingly, Chen et al. reported that the $AA'_3B_2B'_2O_{12}$-type perovskite $CaCu_3Fe_2Re_2O_{12}$ is a half metal with a high Curie temperature up to 560 K.[37] Most recently, another A- and B-site ordered perovskite $CaCu_3Fe_2Os_2O_{12}$ (CCFOO) was discovered.[40] Compared with the double perovskite Ca_2FeOsO_6 with a T_C ∼ 320 K, the T_C of CCFOO sharply increases to 580 K on account of the introduction of Cu^{2+} ions at the A′-site, which leads to strong Cu^{2+}−Fe^{3+} and Cu^{2+}−Os^{5+} spin interactions. Moreover, at the Fermi surface, the electronic density of states of CCFOO is governed by Os^{5+}, whereas Cu^{2+} and Fe^{3+} are far away from the Fermi surface. This indicates that electrical transport can be readily tuned by changing the electric charge of the Os^{5+}-site alone, while high-temperature ferrimagnetism may still be preserved. In this paper, we find that applying hole substitution at the nonmagnetic A-site of CCFOO can significantly change the electronic states of the B′-site Os ions, and therefore, FiM half-metallicity with a T_C above room temperature is found to occur in $NaCu_3Fe_2Os_2O_{12}$ (NCFOO).

2. EXPERIMENTAL AND CALCULATION DETAILS

Polycrystalline $NaCu_3Fe_2Os_2O_{12}$ was synthesized on a cubic-anvil-type high-pressure apparatus at 8−10 GPa and 1573 K for 30 min. High purity (>99.9%) NaOH, CuO, Fe_2O_3, and Os were used as raw materials, and 20 wt % $KClO_4$ was added as the oxygen source. These reactants were finely mixed and ground in a glovebox filled with Ar gas, and then the mixed powders were sealed in a platinum capsule with 3.0 mm diameter and 4.0 mm length for high-pressure treatment. The residual KCl in the product was washed out by deionized water.

Powder X-ray diffraction (XRD) was measured on a G670 imaging plate guinier camera from Huber diffraktionstechnik GmbH & Co. KG. Cu $K\alpha_1$ radiation was used. The scanning range of 2θ is from 10 to 100°, with 0.005° per step. The GSAS program[41] was used to refine the crystallographic parameters. The X-ray absorption spectroscopies (XAS) of Cu-$L_{2,3}$ and Fe-$L_{2,3}$ were adopted at beamline BL08B of the National Synchrotron Radiation Research Center (NSRRC) in Taiwan, using a total electron yield (TEY) mode. The XAS of Os-L_3 was measured at beamline BL07A of NSRRC, using the TEY mode. The X-ray magnetic circular dichroism (XMCD) spectra of Cu-$L_{2,3}$ and Fe-$L_{2,3}$ were recorded at beamline DEIMOS of synchrotron SOLEIL in Paris, with a temperature of 20 K and a magnetic field of 6 T. The XMCD of Os-$L_{2,3}$ was measured at beamline ODE of SOLEIL, with a temperature of 20 K and a magnetic field of 1.2 T. The magnetic properties of NCFOO were measured on a magnetic property measurement system (MPMS3, Quantum Design). Both zero-field-cooling (ZFC) and field-cooling (FC) magnetic susceptibility data were collected under a 0.1 T magnetic field. The resistivity and magnetoresistivity were measured on a physical property measurement system (PPMS7, Quantum Design), using a standard four-probe method. The size of the sample is about 2 × 1 × 1 mm^3 for electrical measurements.

First-principles calculations were carried out. The full-potential linearized augmented plane-wave method was adopted using the WIEN2K package.[42] The crystallographic parameters obtained from the XRD refinement were chosen as the starting parameters. The muffin-tin radii R_{MT} were set as 2.50, 1.90, and 1.60 au for Na, transition metals (Cu, Fe, and Os), and O, respectively. The maximum modulus for the reciprocal vectors K_{max} was chosen following the equation, $R_{MT}K_{max}$ = 8.0. The generalized-gradient approximation with generalized gradient approximation-Perdew−Burke−Ernzerhof (GGA-PBE)[43] exchange−correlation energy was used. For the Brillouin zone, 1000 k-point meshes were taken. For the GGA + U calculations, the effective Coulomb interactions U_{eff} were chosen to be 5, 4, and 2 eV for Cu, Fe, and Os, respectively.

3. RESULTS AND DISCUSSION

The XRD pattern of NCFOO measured at room temperature and the related structural refinement results are shown in Figure 2. Based on the Rietveld analysis, the as-made NCFOO is found to crystallize into both A- and B-site ordered quadruple perovskite with space group $Pn\bar{3}$ (Figure 1c). In this symmetry, Na and Cu occupy the A and A′ sites with a ratio of 1:3, and Fe and Os orderly occupy the B and B′ sites in a rocksalt-type fashion, respectively. The presence of diffraction

DOI: 10.1021/acs.inorgchem.8b02404
Inorg. Chem. 2019, 58, 320−326

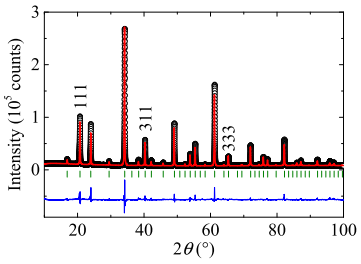

Figure 2. XRD pattern and structural refinement results obtained at room temperature for NCFOO. The observed (black circles), calculated (red line), and difference (bottom line) are shown. The ticks indicate the allowed Bragg reflections with space group $Pn\bar{3}$.

peaks with $h + k + l$ = odd such as (111), (311), and (333) is in good agreement with the rocksalt order of the B/B′-site. The refined results are listed in Table 1. According to the

Table 1. Refined Structural Parameters and Bond-Valence Sum (BVS) Calculations of NCFOO at Room Temperature[a]

parameter	NCFOO
a (Å)	7.410(13)
O_x	0.5679(5)
O_y	0.7608(4)
O_z	0.0596(5)
G (4b for Fe)	0.983(1)
G (4b for Os)	0.017(1)
G (4c for Os)	0.983(1)
G (4c for Fe)	0.017(1)
U_{iso} for Na (100 × Å^2)	0.037(5)
U_{iso} for Cu (100 × Å^2)	0.012(1)
U_{iso} for Fe (100 × Å^2)	0.016(1)
U_{iso} for Os (100 × Å^2)	0.023(1)
U_{iso} for O (100 × Å^2)	0.025(2)
d_{Cu-O} (×4) (Å)	1.954(4)
d_{Fe-O} (×6) (Å)	2.045(4)
d_{Os-O} (×6) (Å)	1.895(4)
∠Fe−O−Os (deg)	140.2(2)
∠Cu−O−Fe (deg)	106.7(1)
∠Cu−O−Os (deg)	113.0(2)
BVS (Cu)	1.90
BVS (Fe)	2.82
R_{wp} (%)	6.64
R_p (%)	4.21

[a]Space group: $Pn\bar{3}$; atomic sites: Na 2a (0.25, 0.25, 0.25); Cu 6d (0.25, 0.75, 0.75); Fe 4b (0, 0, 0); Os 4c (0.5, 0.5, 0.5); O 24h (x, y, z). The BVS values (V_i) were calculated using the formula $V_i = \sum_j S_{ij}$, and $S_{ij} = \exp[(r_0 - r_{ij})/0.37]$. The value of r_0 = 1.679 for Cu and 1.765 for Fe. For B-site Fe, six coordinated oxygen atoms were used. For A′-site Cu, 4 coordinated oxygen atoms were used. G: site occupancy factor.

distances of Cu−O and Fe−O bonds, the bond valence sum (BVS) calculations unveil the Cu^{2+} and Fe^{3+} states, indicating the combination of the $Cu^{2+}/Fe^{3+}/Os^{5.5+}$ charge state in NCFOO, as shown later by XAS measurements. The order degrees of A- and B-site cations are analyzed on the basis of the refined occupancy factors. Na and Cu are assumed to ideally occupy the A-site and the A′-site, respectively, due to the large difference in ionic size as well as the strong Jahn−Teller effect of Cu^{2+}, which is required to form the square-planar coordinated $A'O_4$ units. Therefore, we fix the occupancy factors of Na and Cu to be unity to study the B/B′-site order degree. The refinement shows that there is a small amount of Fe−Os anti-site occupancy by about 1.7%.

The valence states of transition metals can be determined by XAS measurement.[44−46] Figure 3a,b shows the Cu- and Fe-$L_{2,3}$

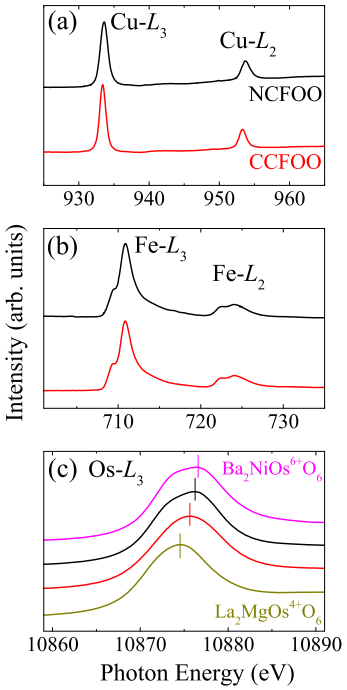

Figure 3. XAS of (a) Cu-$L_{2,3}$ edges, (b) Fe-$L_{2,3}$ edges, and (c) Os-L_3 edges. The XAS of some related references are also shown for comparison. The vertical lines in (c) from bottom to top show the gradual variation of the valence state from Os^{4+} to Os^{6+}.

XAS spectra of NCFOO. For comparison, the isostructural CCFOO with determined $Cu^{2+}/Fe^{3+}/Os^{5+}$ charge combination is used as a standard reference. Obviously, both the Cu- and Fe-$L_{2,3}$ edges of NCFOO exhibit very similar spectral features such as similar peak energy position and spectral shape with those of CCFOO, revealing the formation of Cu^{2+} and Fe^{3+} in NCFOO. To identify the valence state of Os, the B-site ordered double perovskites La_2MgOsO_6 and Ba_2NiOsO_6 are also adopted as Os^{4+} and Os^{6+} references, respectively,[47] in addition to the Os^{5+} reference of CCFOO. As shown in Figure 3c, upon increasing the valence state from Os^{4+} to Os^{6+}, the energy position of the Os-L_3 edge systematically shifts toward higher energies. Specifically, the energy position of NCFOO is located at the intermediate between the Os^{5+} CCFOO and Os^{6+} Ba_2NiOsO_6 references. Therefore, an average $Os^{5.5+}$ valence state is assigned for NCFOO, as required by charge conservation. This fractional charge state means that the Os-site should be mixed by disordered Os^{5+} and Os^{6+} ions with a 1:1 ratio, as required by the $Pn\bar{3}$ space group.

The magnetism of NCFOO was studied by magnetization and magnetic susceptibility measurements. Figure 4a presents the field-dependent magnetization of NCFOO at different temperatures. Obviously, these compounds display canonical magnetic hysteresis loops at 300 K, suggesting the strong FM or FiM spin interactions as well as the resulting high T_C in NCFOO. A saturated moment of 5.5 μ_B/fu is observed at 2 K and 7 T. Furthermore, Figure 4b displays the ZFC and FC

DOI: 10.1021/acs.inorgchem.8b02404
Inorg. Chem. 2019, 58, 320−326

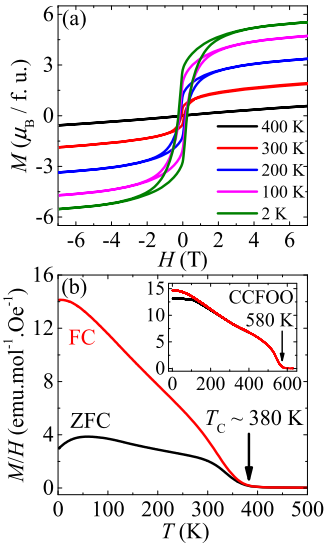

Figure 4. (a) Field-dependent magnetization measured at different temperatures for NCFOO. (b) Temperature-dependent magnetic susceptibility measured at 0.1 T with ZFC and FC modes for NCFOO. The inset shows the magnetic susceptibility of CCFOO for comparison.

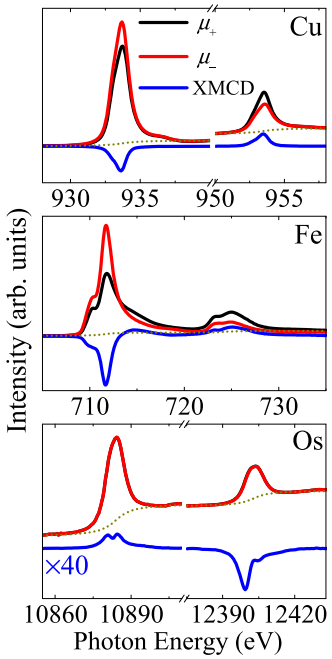

Figure 5. XMCD of Fe-$L_{2,3}$, Cu-$L_{2,3}$, and Os-$L_{2,3}$ edges for NCFOO. The photon spin is aligned parallel (μ^+ black line) and antiparallel (μ^- red line) to the applied magnetic field, respectively. The difference spectra are shown in blue.

magnetic susceptibility curves. As the temperature decreases, the susceptibility experiences an apparent increase at $T_C \sim 380$ K. The current NCFOO thus possesses a high T_C well above room temperature. Compared with the isostructural compound CCFOO (inset of Figure 4b), the T_C of NCFOO is reduced clearly. This can be mainly attributed to the decrease of the d-electron amount in an average $Os^{5.5+}$ ion with regard to an Os^{5+} ion, which will weaken the superexchange spin interactions of Cu−O−Os and Fe−O−Os.

Since there are three magnetic ions (Cu^{2+}, Fe^{3+}, and $Os^{5.5+}$) in NCFOO, all of them possibly involved in the spin interactions. When we consider the spin-only contribution in the assumption of a localized electronic model with Cu^{2+}/Fe^{3+}/$Os^{5.5+}$ charge combination, in theory, the saturated spin moment generated by the collinear $Cu^{2+}(\uparrow)Fe^{3+}(\uparrow)Os^{5.5+}(\uparrow)$ FM alignment (18 μ_B/fu) and the FiM $Cu^{2+}(\uparrow)Fe^{3+}(\downarrow)$-$Os^{5.5+}(\downarrow)$ (12 μ_B/fu) and $Cu^{2+}(\uparrow)Fe^{3+}(\downarrow)Os^{5.5+}(\uparrow)$ (2 μ_B/fu) couplings are all far away from the measurement data mentioned above at 2 K. In comparison, only the $Cu^{2+}(\uparrow)$-$Fe^{3+}(\uparrow)Os^{5.5+}(\downarrow)$ FiM configuration (8 μ_B/fu) results in comparable spin moment with experiment (5.5 μ_B/fu). The difference comes from the strong p−d hybridization effect between oxygen and Os as well as the spin-orbital coupling (SOC) of the 5d $Os^{5.5+}$ electrons (shown later). In addition, the Fe−Os anti-site occupancy (∼1.7%) can also reduce the saturated moment.

To further confirm the $Cu^{2+}(\uparrow)Fe^{3+}(\uparrow)Os^{5.5+}(\downarrow)$ FiM coupling, we performed XMCD measurements on NCFOO. This element-selective method can provide information of magnetic coupling between any two elements in a compound, even the sample is not fully magnetically saturated.[48,49] Figure 5 shows the related results. Obviously, the XMCD spectra of NCFOO display the same negative (positive) sign at the L_3 (L_2) edges for Cu and Fe, whereas the inverse signs are observed for Os, providing convincing evidence for the proposed $Cu^{2+}(\uparrow)Fe^{3+}(\uparrow)Os^{5.5+}(\downarrow)$ FiM coupling. Using the sum rules,[50−53] we estimated the total magnetic moment of 6.8 ± 0.3 μ_B for per NCFOO, which is similar to the saturated magnetic moment observed at 2 K.

The electrical transport properties of NCFOO are characterized by electrical resistivity (ρ) and magnetoresistance [MR = 100% × ($\rho(H) - \rho(0)$)/$\rho(0)$]. Figure 6a displays the temperature-dependent resistivity measured at 0 and 8 T as well as the MR between them. One finds that the

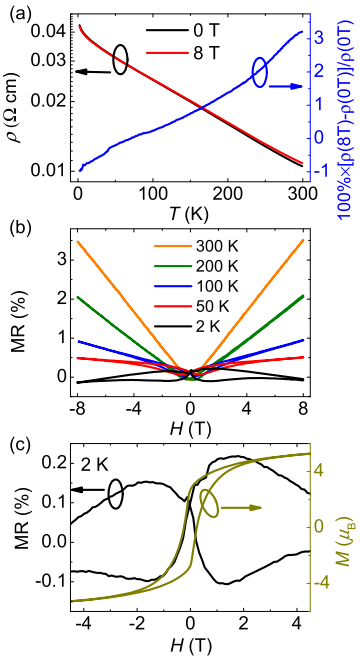

Figure 6. (a) Temperature dependence of the resistivity and magnetoresistance of NCFOO. (b) Magnetic-field dependence of magnetoresistance at selected temperatures. (c) Field dependence of magnetoresistance and magnetization measured at 2 K.

DOI: 10.1021/acs.inorgchem.8b02404
Inorg. Chem. 2019, 58, 320−326

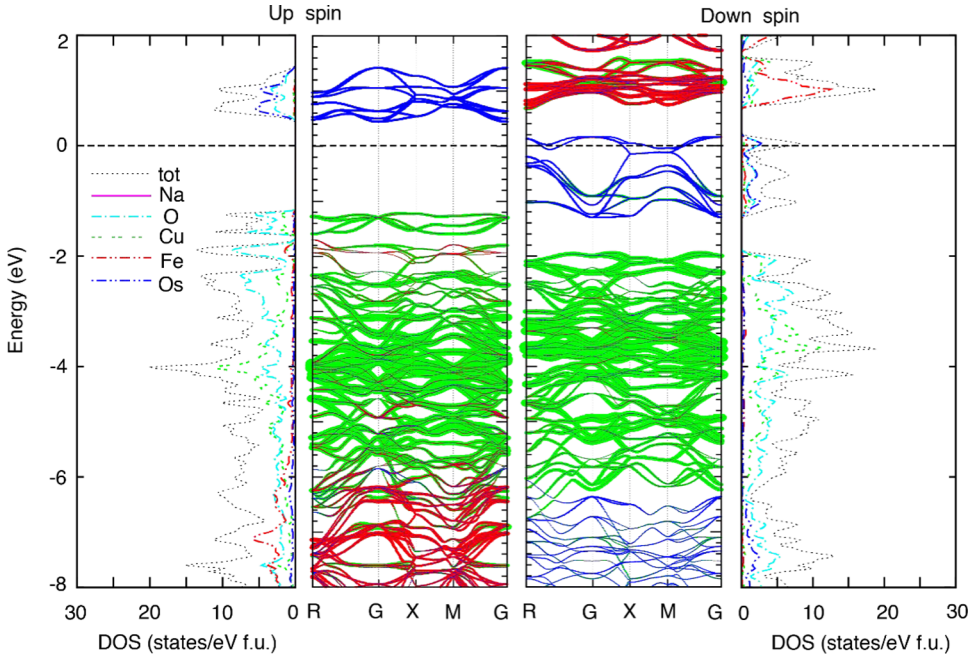

Figure 7. First-principles numerical results for the band structures and partial densities of states of NCFOO within GGA + *U*.

resistivity of NCFOO is at the level of 10^{-2} Ω cm at room temperature, and slightly increases upon cooling to about 0.04 Ω cm at 2 K. Considering the polycrystalline nature of CCFOO, where grain boundary scattering effects play some roles in resistance, this slightly temperature-raised resistivity behavior may imply half-metallic conductivity as observed in other polycrystalline half metals.[6,54] In addition, the MR changes the sign from positive to negative around 50 K (Figure 6a,b). When we plot the MR and MH curves measured at 2 K (Figure 6c), the butterfly-shaped MR curve is found to occur. Moreover, the hysteresis field presented in MR is much larger than that in MH, probably suggesting the spin-valve-type MR behavior of NCFOO arising from the intergrain tunneling of spin-polarized conduction carriers as reported in the well-studied half metal of Sr_2FeMoO_6 ceramic[6,55] and the quadruple perovskite $CaCu_3Fe_2Re_2O_{12}$.[37] However, in comparison, the MR value of NCFOO is considerably reduced probably due to the strong magnetic frustration as mentioned in ref 40 as well as the small amount of Fe−Os disorder effects.

To further unveil the possible half-metallic properties for NCFOO, we carried out first-principles theoretical calculations. To confirm the magnetic ground state, GGA, GGA + *U*, and GGA + *U* + SOC spin-polarized calculations were performed for all of the four possible magnetic configurations, i.e., $Cu^{2+}(\uparrow)Fe^{3+}(\uparrow)Os^{5.5+}(\downarrow)$, $Cu^{2+}(\uparrow)Fe^{3+}(\downarrow)Os^{5.5+}(\downarrow)$, $Cu^{2+}(\uparrow)Fe^{3+}(\downarrow)Os^{5.5+}(\uparrow)$, and $Cu^{2+}(\uparrow)Fe^{3+}(\uparrow)Os^{5.5+}(\uparrow)$. The GGA calculations always converge to the FiM $Cu^{2+}(\uparrow)$-$Fe^{3+}(\uparrow)Os^{5.5+}(\downarrow)$ ground state. The GGA + *U* calculations also give the same results, in coherence with the experiment. However, only the first two configurations remain stable and converge to themselves, whereas the latter two become unstable during the self-consistent iterations and always converge to the FiM $Cu^{2+}(\uparrow)Fe^{3+}(\uparrow)Os^{5.5+}(\downarrow)$ state. For simplicity, we only present the results using U_{eff} = 5, 4, and 2 eV for Cu, Fe, and Os, respectively, according to the literature.[40] We also tried many other choices of U_{eff} around the above values, and the conclusion is qualitatively unchanged. Compared to the FiM $Cu^{2+}(\uparrow)Fe^{3+}(\downarrow)Os^{5.5+}(\downarrow)$ spin configuration, the energy of the $Cu^{2+}(\uparrow)Fe^{3+}(\uparrow)Os^{5.5+}(\downarrow)$ state is lower to about 623.22 meV/fu, indicating that the latter is a very stable magnetic ground state, agreeing well with the XMCD measurement.

The spin and valence states of Os can also be obtained from the calculations. The calculated moments using GGA + *U* are 0.593 μ_B/Cu, 4.097 μ_B/Fe, −1.143 μ_B/Os, and 0.064 μ_B/O inside the muffin-tin spheres, generating a total magnetic moment of 8.0 μ_B/fu including the interstitial contributions. Since the typical moments are 1.0 μ_B for Cu^{2+} and 5.0 μ_B for Fe^{3+}, one immediately obtains the moment of Os to be 2.5 μ_B, and the average valence state has to be $Os^{5.5+}$. This leads to the rational conclusion that $Os^{5.5+}$ is in a fully polarized spin state. The GGA + *U* + SOC calculations are also performed. The results are essentially similar to those of GGA + *U* calculations, except that the B′-site Os shows a considerable orbital moment. The calculated Os spin (orbit) moments are −1.082 (0.137) μ_B inside the muffin-tin spheres. The orbital moment is about 13% of the spin moment, suggesting a stronger SOC effect in NCFOO.

Figure 7 shows the band structures as well as the density of states near the Fermi level calculated with the U_{eff} values mentioned above. The half-metallic feature of NCFOO is clearly seen from the band structures, where only the Os bands cross the Fermi energy. Specifically, the minority (spin-down) channel is conducting, whereas the majority (spin-up) channel has a rather wide energy gap of about 1.6 eV. The above conclusions are qualitatively unchanged with varying U_{eff} values, and a half-metal is obtained even in GGA calculations at U_{eff} = 0, except that the band gap in majority spin is reduced than that in GGA + *U*. In GGA + *U*, the Coulomb interaction is treated in a mean-field manner. As expected, it decreases the energy of the occupied bands and increases the energy of the unoccupied bands. Thus, the empty and fully occupied Fe and Cu bands are pushed away, so that the partially filled Os bands become dominant around the Fermi energy. As a consequence, the energy gap in the majority spin channel is enlarged in GGA + *U*, and the metallic behavior of the minority spin channel

DOI: 10.1021/acs.inorgchem.8b02404
Inorg. Chem. 2019, 58, 320−326

becomes solely associated with the Os bands. The electronic correlations in NCFOO thus play the role of protecting the half-metallic state by increasing the band gap in the majority spin channel.

4. CONCLUSIONS

In summary, we succeeded in preparing a new oxide $NaCu_3Fe_2Os_2O_{12}$ at 8−10 GPa and 1573 K. This compound is determined to be both A- and B-site ordered quadruple perovskite with a space group of $Pn\bar{3}$. Rietveld refinement indicates that Na at the A-site and Cu at the A′-site are almost ideally 1:3 ordered, and slight (∼1.7%) anti-site occupancies are found between the Fe at the B-site and Os at the B′-site. According to the BVS calculations and XAS results, the charge states are determined to be $Cu^{2+}/Fe^{3+}/Os^{5.5+}$. A high T_C of about 380 K is observed because of the strong FiM coupling between the transition metal cations, as revealed by XMCD measurements and first-principles calculations. Different from the semiconducting parent compound CCFOO, the hole-substituted NCFOO exhibits half-metallic properties possessing a high T_C and a wide energy gap. The present work provides an interesting example of how to design promising half metals in $AA'_3B_2B'_2O_{12}$-type ordered quadruple perovskite oxides.

AUTHOR INFORMATION

Corresponding Authors

*E-mail: ywlong@iphy.ac.cn (Y.L.).
*E-mail: yifeng@iphy.ac.cn (Y.-F.Y.).

ORCID

Min Liu: 0000-0002-7674-7309
Yun-Liang Soo: 0000-0002-1683-3141
Youwen Long: 0000-0002-8587-7818

Funding

This work was supported by the National Natural Science Foundation of China (Grant no. 51772324, 11574378 and 11522435), the National Key R&D Program of China (Grant no. 2018YFA0305700 and 2015CB921303), and the Chinese Academy of Sciences (Grant no. QYZDB-SSW-SLH013, YZ201555, GJHZ1773, XDB07030300 and XDB07020200).

Notes

The authors declare no competing financial interest.

ACKNOWLEDGMENTS

The authors thank Prof. L. H. Tjeng for fruitful discussion and valuable suggestion.

REFERENCES

(1) Žutić, I.; Fabian, J.; Das Sarma, S. Spintronics: Fundamentals and Applications. *Rev. Mod. Phys.* **2004**, *76*, 323−410.
(2) Katsnelson, M. I.; Irkhin, V. Y.; Chioncel, L.; Lichtenstein, A. I.; de Groot, R. A. Half-Metallic Ferromagnets: From Band Structure to Many-Body Effect. *Rev. Mod. Phys.* **2008**, *80*, 315−378.
(3) Fert, A. Noble Lecture: Origin, Development, and Future of Spintronics. *Rev. Mod. Phys.* **2008**, *80*, 1517−1530.
(4) Wang, X.-L.; Dou, S. X.; Zhang, C. Zero-Gap Materials for Future Spintronics, Electronics and Optics. *NPG Asia Mater.* **2010**, *2*, 31−38.
(5) de Groot, R. A.; Mueller, F. M.; van Engen, P. G.; Buschow, K. H. J. New Class of Materials: Half-Metallic Ferromagnets. *Phys. Rev. Lett.* **1983**, *50*, 2024−2027.
(6) Kobayashi, K.-I; Kimura, T.; Sawada, H.; Terakura, K.; Tokura, Y. Room-Temperature Magnetoresistance in an Oxide Material with an Ordered Double-Perovskite Structure. *Nature* **1998**, *395*, 677−680.
(7) Xie, W.-H; Xu, Y.-Q; Liu, B.-G; Pettifor, D. G. Half-Metallic Ferromagnetism and Structural Stability of Zincblende Phases of the Transition-Metal Chalcogenides. *Phys. Rev. Lett.* **2003**, *91*, No. 037204.
(8) Galanakis, I.; Mavropoulos, P.; Dederichs, P. H. Electronic Structure and Slater-Pauling Behaviour in Half-Metallic Heusler Alloys Calculated form First Principles. *J. Phys. D: Appl. Phys.* **2006**, *39*, 765−775.
(9) Galanakis, I.; Mavropoulos, P. Spin-Polarization and Electronic Properties of Half-Metallic Heusler Alloys Calculated from First Principles. *J. Phys.: Condens. Matter* **2007**, *19*, No. 315213.
(10) Li, X.; Wu, X.; Yang, J. Room-Temperature Half-Metallicity in La(Mn,Zn)AsO Alloy via Element Substitutions. *J. Am. Chem. Soc.* **2014**, *136*, 5664−5669.
(11) Li, X.; Wu, X.; Yang, J. Half-Metallicity in $MnPSe_3$ Exfoliated Nanosheet with Carrier Doping. *J. Am. Chem. Soc.* **2014**, *136*, 11065−11069.
(12) Li, M.-R; Retuerto, M.; Deng, Z.; Stephens, P. W.; Croft, M.; Huang, Q.; Wu, H.; Deng, X.; Kotliar, G.; Sanchez-Benitez, J.; Hadermann, J.; Walker, D.; Greenblatt, M. Giant Magnetoresistance in the Half-Metallic Double-Perovskite Ferrimagnet Mn_2FeReO_6. *Angew. Chem., Int. Ed.* **2015**, *54*, 12069−12073.
(13) Meng, J.; Zhang, L.; Yao, F.; Zhang, X.; Zhang, W.; Liu, X.; Meng, J.; Zhang, H. Theoretical Study on the Negative Thermal Expansion Perovskite $LaCu_3Fe_4O_{12}$: Pressure-Triggered Transition of Magnetism, Charge, and Spin State. *Inorg. Chem.* **2017**, *56*, 6371−6379.
(14) Chandra, H. K.; Guo, G.-Y. Quantum Anomalous Hall Phase and Half-Metallic Phase in Ferromagnetic (111) Bilayers of 4*d* and 5*d* Transition Metal Perovskites. *Phys. Rev. B* **2017**, *95*, No. 134448.
(15) Park, J.-H; Vescovo, E.; Kim, H.-J; Kwon, C.; Ramesh, R.; Venkatesan, T. Direct Evidence for a Half-Metallic Ferromagnet. *Nature* **1998**, *392*, 794−796.
(16) Nadgorny, B.; Mazin, I. I.; Osofsky, M.; Soulen, R. J.; Broussard, P.; Stroud, R. M.; Singh, D. J.; Harris, V. G.; Arsenov, A.; Mukovskii, Y. Origin of High Transport Spin Polarization in $La_{0.7}Sr_{0.3}MnO_3$: Direct Evidence for Minority Spin States. *Phys. Rev. B* **2001**, *63*, No. 184433.
(17) Wu, S. M.; Cybart, S. A.; Yu, P.; Rossell, M. D.; Zhang, J. X.; Ramesh, R.; Dynes, R. C. Reversible Electric Control of Exchange Bias in a Multiferroic Field-Effect Device. *Nat. Mater.* **2010**, *9*, 756−761.
(18) Sarma, D. D.; Mahadevan, P.; Saha-Dasgupta, T.; Ray, S.; Kumar, A. Electronic Structure of Sr_2FeMoO_6. *Phys. Rev. Lett.* **2000**, *85*, 2549−2552.
(19) Tomioka, Y.; Okuda, T.; Okimoto, Y.; Kumai, R.; Kobayashi, K.-I.; Tokura, Y. Magnetic and Electronic Properties of a Single Crystal of Ordered Double Perovskite Sr_2FeMoO_6. *Phys. Rev. B* **2000**, *61*, 422−427.
(20) Pickett, W. E. Spin-Density-Functional-Based Search for Half-Metallic Antiferromagnets. *Phys. Rev. B* **1998**, *57*, 10613−10619.
(21) Chakraverty, S.; Yoshimatsu, K.; Kozuka, Y.; Kumigashira, H.; Oshima, M.; Makino, T.; Ohtomo, A.; Kawasaki, M. Magnetic and Electronic Properties of Ordered Double-Perovskite La_2VMnO_6 Thin Films. *Phys. Rev. B* **2011**, *84*, No. 132411.
(22) Barón-González, A. J.; Frontera, C.; García-Muñoz, J. L.; Rivas-Murias, B.; Blasco, J. Effect of Cation Disorder on Structural, Magnetic and Dielectric Properties of La_2MnCoO_6 Double Perovskite. *J. Phys.: Condens. Matter* **2011**, *23*, No. 496003.
(23) Lee, K.-W.; Ahn, K.-H. Evaluation of Half-Metallic Antiferromagnetism in A_2CrFeO_6 (A = La, Sr). *Phys. Rev. B* **2012**, *85*, No. 224404.
(24) Samanta, K.; Sanyal, P.; Saha-Dasgupta, T. Half-Metallic Behavior in Doped Sr_2CrOsO_6 Double Perovskite with High Transition Temperature. *Sci. Rep.* **2015**, *5*, No. 15010.
(25) Carpenter, M. A.; Howard, C. J. Symmetry Rules and Strain/Order-Parameter Relationship for Coupling between Octahedral

DOI: 10.1021/acs.inorgchem.8b02404
Inorg. Chem. 2019, 58, 320−326

Tilting and Cooperative Jahn-Teller Transitions in ABX_3 Perovskite. I. Theory. *Acta Crystallogr., Sect. B: Struct. Sci.* **2009**, *65*, 134−146.
(26) King, G.; Woodward, P. M. Cation Ordering in Perovskites. *J. Mater. Chem.* **2010**, *20*, 5785−5796.
(27) Vasala, S.; Karppinen, M. $A_2B'B''O_6$ Perovskites: A Review. *Prog. Solid State Chem.* **2015**, *43*, 1−36.
(28) Prodi, A.; Gilioli, E.; Gauzzi, A.; Licci, F.; Marezio, M.; Bolzoni, F.; Huang, Q.; Santoro, A.; Lynn, J. W. Charge, Orbital and Spin Ordering Phenomena in the Mixed Valence Manganite $(NaMn_3^{3+})$-$(Mn_2^{3+}Mn_2^{4+})O_{12}$. *Nat. Mater.* **2004**, *3*, 48−52.
(29) Long, Y. W.; Hayashi, N.; Saito, T.; Azuma, M.; Muranaka, S.; Shimakawa, Y. Temperature-Induced *A*-*B* Intersite Charge Transfer in an *A*-Site-Ordered $LaCu_3Fe_4O_{12}$ Perovskite. *Nature* **2009**, *458*, 60−63.
(30) Chen, W.-T; Mizumaki, M.; Saito, T.; Shimakawa, Y. Frustration Relieved Ferrimagnetism in Novel *A*- and *B*-Site-Ordered Quadruple Perovskite. *Dalton Trans.* **2013**, *42*, 10116−10120.
(31) Wang, X.; Chai, Y. S.; Zhou, L.; Cao, H. B.; Cruz, C.-D; Yang, J. Y.; Dai, J. H.; Yin, Y. Y.; Yuan, Z.; Zhang, S. J.; Yu, R. Z.; Azuma, M.; Shimakawa, Y.; Zhang, H. M.; Dong, S.; Sun, Y.; Jin, C. Q.; Long, Y. W. Observation of Magnetoelectric Multiferroicity in a Cubic Perovskite System: $LaMn_3Cr_4O_{12}$. *Phys. Rev. Lett.* **2015**, *115*, No. 087601.
(32) Yamada, I.; Murakami, M.; Hayashi, N.; Mori, S. Inverse Charge Transfer in the Quadruple Perovskite $CaCu_3Fe_4O_{12}$. *Inorg. Chem.* **2016**, *55*, 1715−1719.
(33) Sakai, Y.; Yang, J. Y.; Yu, R.; Hojo, H.; Yamada, I.; Miao, P.; Lee, S.; Torii, S.; Kamiyama, T.; Lezaic, M.; Bihlmayer, G.; Mizumaki, M.; Komiyama, J.; Mizokawa, T.; Yamamoto, H.; Nishikubo, T.; Hattori, Y.; Oka, K.; Yin, Y. Y.; Dai, J. H.; Li, W. M.; Ueda, S.; Aimi, A.; Mori, D.; Inaguma, Y.; Hu, Z. W.; Uozumi, T.; Jin, C. Q.; Long, Y. W.; Azuma, M. *A*-Site and *B*-Site Charge Ordering in an *s*-*d* Level Controlled Perovskite Oxide $PbCoO_3$. *J. Am. Chem. Soc.* **2017**, *139*, 4574−4581.
(34) Byeon, S.-H; Lufaso, M. W.; Parise, J. B.; Woodward, P. M.; Hansen, T. High-Pressure Synthesis and Characterization of Perovskites with Simultaneous Ordering of Both the *A*- and *B*-Site Cations, $CaCu_3Ga_2M_2O_{12}$ (M = Sb, Ta). *Chem. Mater.* **2003**, *15*, 3798−3804.
(35) Byeon, S.-H; Lee, S.-S; Parise, J. B.; Woodward, P. M.; Hur, N. H. New Ferrimagnetic Oxide $CaCu_3Cr_2Sb_2O_{12}$: High-Pressure Synthesis, Structure, and Magnetic Properties. *Chem. Mater.* **2005**, *17*, 3552−3557.
(36) Byeon, S.-H; Lee, S.-S; Parise, J. B.; Woodward, P. M. New Perovskite Oxide $CaCu_3Cr_2Ru_2O_{12}$: Comparison with Structural, Magnetic, and Transport Properties of the $CaCu_3B'_2B''_2O_{12}$ Perovskite Family. *Chem. Mater.* **2006**, *18*, 3873−3877.
(37) Chen, W.-T; Mizumaki, M.; Seki, H.; Senn, M. S.; Saito, T.; Kan, D.; Attfield, J. P.; Shimakawa, Y. A Half-Metallic *A*- and *B*-Site-Ordered Quadruple Perovskite Oxide $CaCu_3Fe_2Re_2O_{12}$ with Large Magnetization and a High Transition Temperature. *Nat. Commun.* **2014**, *5*, No. 3909.
(38) Larregola, S. A.; Zhou, J.; Alonso, J. A.; Pomjakushin, V.; Goodenough, J. B. New Routes to Synthesizing an Ordered Perovskite $CaCu_3Fe_2Sb_2O_{12}$ and Its Magnetic Structure by Neutron Powder Diffraction. *Inorg. Chem.* **2014**, *53*, 4281−4283.
(39) Yin, Y.-Y; Liu, M.; Dai, J.-H; Wang, X.; Zhou, L.; Cao, H.; dela Cruz, C.; Chen, C.-T; Xu, Y.; Shen, X.; Yu, R.; Alonso, J. A.; Muñoz, A.; Yang, Y.-F; Jin, C.; Hu, Z.; Long, Y. W. $LaMn_3Ni_2Mn_2O_{12}$: An *A*- and *B*-Site Ordered Quadruple Perovskite with *A*-Site Tuning Orthogonal Spin Ordering. *Chem. Mater.* **2016**, *28*, 8988−8996.
(40) Deng, H. S.; Liu, M.; Dai, J. H.; Hu, Z. W.; Kuo, C. Y.; Yin, Y. Y.; Yang, J. Y.; Wang, X.; Zhao, Q.; Xu, Y. J.; Fu, Z. M.; Cai, J. W.; Guo, H. Z.; Jin, K. J.; Pi, T. W.; Soo, Y.; Zhou, G. H.; Cheng, J. G.; Chen, K.; Ohresser, P.; Yang, Y. F.; Jin, C. Q.; Tjeng, L. H.; Long, Y. W. Strong Enhancement of Spin Ordering by *A*-Site Magnetic Ions in the Ferrimagnet $CaCu_3Fe_2Os_2O_{12}$. *Phys. Rev. B* **2016**, *94*, No. 024414.
(41) Larson, A. C.; Von Dreele, R. B. *General Structure Analysis System (GSAS)*; Report No. LAUR 86−748; Los Alamos National Laboratory: Los Alamos, NM, 1994.
(42) Blaha, P.; Schwarz, K.; Madsen, G. K. H.; Kvasnicka, D.; Luitz, J. *WIEN2K: An Augmented Plane Wave+Local Orbitals Program for Calculating Crystal Properties*; Karlheinz Schwarz, Technische Universitat Wien: Wien, Austria, 2013.
(43) Perdew, J. P.; Burke, K.; Ernzerhof, M. Generalized Gradient Approximation Made Simple. *Phys. Rev. Lett.* **1996**, *77*, 3865−3868.
(44) Choy, J.-H; Kim, D.-K; Hwang, S.-H; Demazeau, G.; Jung, D.-Y XANES and EXAFS Studies on the Ir-O Bond Covalency in Ionic Iridium Perovskites. *J. Am. Chem. Soc.* **1995**, *117*, 8557−8566.
(45) Hu, Z.; Golden, M. S.; Ebbinghaus, S. G.; Knupfer, M.; Fink, J.; de Groot, F. M. F.; Kaindl, G. The Distribution of the Doped Holes in $La_{2-x}Sr_xCu_{1-y}Ru_yO_{4-\delta}$. *Chem. Phys.* **2002**, *282*, 451−463.
(46) Nemrava, S.; Vinnik, D. A.; Hu, Z. W.; Valldor, M.; Kuo, C.-Y; Zherebtsov, D. A.; Gudkova, S. A.; Chen, C.-T; Tjeng, L.-H; Niewa, R. Three Oxidation States of Manganese in the Barium Hexaferrite $BaFe_{12-x}Mn_xO_{19}$. *Inorg. Chem.* **2017**, *56*, 3861−3866.
(47) Feng, H. L.; Calder, S.; Ghimire, M. P.; Yuan, Y.-H; Shirako, Y.; Tsujimoto, Y.; Matsushita, Y.; Hu, Z. W.; Kuo, C.-Y; Tjeng, L. H.; Pi, T.-W; Soo, Y.-L; He, J.; Tanaka, M.; Katsuya, Y.; Richter, M.; Yamaura, K. Ba_2NiOsO_6: A Dirac-Mott Insulator with Ferromagnetism near 100 K. *Phys. Rev. B* **2016**, *94*, No. 235158.
(48) Burnus, T.; Hu, Z.; Hsieh, H. H.; Joly, V. L. J.; Joy, P. A.; Haverkort, M. W.; Wu, H.; Tanaka, A.; Lin, H.-J; Chen, C. T.; Tjeng, L. H. Local Electronic Structure and Magnetic Properties of $LaMn_{0.5}Co_{0.5}O_3$ Studied by X-Ray Absorption and Magnetic Circular Dichroism Spectroscopy. *Phys. Rev. B* **2008**, *77*, No. 125124.
(49) Burnus, T.; Hu, Z.; Wu, H.; Cezar, J. C.; Niitaka, S.; Takagi, H.; Chang, C. F.; Brookes, N. B.; Lin, H.-J; Jang, L. Y.; Tanaka, A.; Liang, K. S.; Chen, C. T.; Tjeng, L. H. X-Ray Absorption and X-Ray Magnetic Dichroism Study on Ca_3CoRhO_6 and Ca_3FeRhO_6. *Phys. Rev. B* **2008**, *77*, No. 205111.
(50) Thole, B. T.; Carra, P.; Sette, F.; van der Laan, G. X-Ray Circular Dichroism as a Probe of Orbital Magnetization. *Phys. Rev. Lett.* **1992**, *68*, 1943−1946.
(51) Carra, P.; Thole, B. T.; Altarelli, M.; Wang, X. D. X-Ray Circular Dichroism and Local Magnetic Fields. *Phys. Rev. Lett.* **1993**, *70*, 694−697.
(52) Chen, C. T.; Idzerda, Y. U.; Lin, H.-J; Smith, N. V.; Meigs, G.; Chaban, E.; Ho, G. H.; Pellegrin, E.; Sette, F. Experimental Confirmation of the X-Ray Magnetic Circular Dichroism Sum Rules for Iron and Cobalt. *Phys. Rev. Lett.* **1995**, *75*, 152−155.
(53) Piamonteze, C.; Mietdema, P.; de Groot, F. M. F. Accuracy of the Spin Sum Rule in XMCD for the Transition-Metal *L* Edges from Manganese to Copper. *Phys. Rev. B* **2009**, *80*, No. 184410.
(54) Chmaissem, O.; Kruk, R.; Dabrowski, B.; Brown, D. E.; Xiong, X.; Kolesnik, S.; Jorgensen, J. D.; Kimball, C. W. Structural Phase Transition and the Electronic and Magnetic Properties of Sr_2FeMoO_6. *Phys. Rev. B* **2000**, *62*, 14197−14206.
(55) Ziese, M. Extrinsic Magnetotransport Phenomena in Ferromagnetic Oxides. *Rep. Prog. Phys.* **2002**, *65*, 143−249.

DOI: 10.1021/acs.inorgchem.8b02404
Inorg. Chem. 2019, 58, 320−326